



Supplementary Materials for

Lineage-dependent spatial and functional organization of the mammalian enteric nervous system

Reena Lasrado, Werend Boesmans,* Jens Kleinjung,* Carmen Pin,* Donald Bell, Leena Bhaw, Sarah McCallum, Hui Zong, Liqun Luo, Hans Clevers, Pieter Vanden Berghe, Vassilis Pachnis†

*These authors contributed equally to this work.

†Corresponding author. Email: vassilis.pachnis@crick.ac.uk

Published 19 May 2017, *Science* **356**, 722 (2017)
DOI: 10.1126/science.aam7511

This PDF file includes:

Materials and Methods
Supplementary Text
Figs. S1 to S7
Tables S1 and S2
Captions for Movies S1 to S4
References

Other Supplementary Material for this manuscript includes the following:
(available at www.sciencemag.org/content/356/6339/722/suppl/DC1)

Movies S1 to S4

Materials and Methods

Animals

All animal procedures were carried out in accordance with the regulatory standards of the UK Home Office and approved by the Animal Welfare and Ethics Review Body (AWERB) of The Francis Crick Institute.

The following transgenic drivers and reporters have been described previously: *Sox10::CreER^{T2}* (SER26; MGI:5301107) (4), *Sox10::Cre* (MGI:J:99989) (23), *Rosa26R-EYFP* (MGI: 2449038) (5), *Rosa26R-Confetti* (MGI:4835542) (6) and *Rosa26-tdT* (MGI: 3809524) (7). *Sox10::CreER^{T2}* (SER93) transgenics were generated by pronuclear microinjection of the Phage Artificial Chromosome (PAC) construct used to establish the *Sox10::CreER^{T2}* (SER26) line (4). In comparison to SER26, SER93 has identical cell type distribution but is less efficient in that only 60-70% of Sox10-expressing cells are labelled following tamoxifen administration. Importantly, no background labelling of Sox10⁺ cells is detected in this line, thus providing control of the timing and number of ENS progenitors labelled in response to limiting doses of tamoxifen (fig. S1). The *MADM6-GR* (MGI:3623347) and *MADM6-RG* (MGI:3623346) alleles of the *Rosa26* locus have been described previously (22). Sox10Cre|MADM mice were generated by breeding the *Sox10::Cre* transgene onto compound *MADM6-GR/MADM6-RG* heterozygotes. To generate Sox10Cre|MADM-*Ret*^{k-} mice, we used meiotic recombination to link the telomeric *Ret*^{k-} (null) allele (MGI:2136894) (25) to the *MADM-GR* allele. For this, homozygous *MADM6-GR* and heterozygous *Ret*^{k-} mice were intercrossed to generate *MADM6-GR;Ret*^{k-} double heterozygotes (F1) which were then crossed with wild-type animals. Inheritance of both the *MADM6-GR* and *Ret*^{k-} alleles in F2 progeny indicated generation of the *MADM6-GR;Ret*^{k-} recombinant allele. The frequency of recombination (3.33%; n=60) was close to the value expected from the distance between *Ret* and *Rosa26* (2.13cM; www.ensembl.org). Sox10Cre|MADM-*Ret*^{k-} mice were subsequently generated by breeding the *Sox10::Cre* allele onto the compound heterozygous *MADM6-GR-Ret*^{k-}/*MADM6-RG* background. Mice of the desired developmental stage were generated by setting up timed pregnancies. The plug day was designated as E0.5 and date of birth as P0. Genotyping was carried out by PCR (genotyping primers used are listed in table S2) and detailed protocols are described in the relevant publication.

Tamoxifen administration

Tamoxifen (Sigma, T-5648) was prepared at a stock concentration of 10 or 20 mg/ml in corn oil/10% ethanol and was administered intraperitoneally. The optimal amount for sparse labelling of E12.5 ENCCs in SER93|EYFP or SER93|Confetti embryos was determined in pilot studies in which a range of doses (2-100µg/g of dam body weight) was administered to pregnant mice (fig. S1). 2µg and 10µg of tamoxifen per gr of dam body weight resulted reproducibly in the formation of well separated distinct ENCC clusters in SER93|EYFP and SER93|Confetti embryos, respectively. Dose of 40µg/g dam body weight was used to generate overlapping clones in the gut of SER93|Confetti mice. The dose of 100µg/gr of dam body weight was chosen in all cases we wished to label the maximum number of ENCCs.

FACS analysis for quantification of ENS cells in the small intestine of mouse embryos

E12.5 SER26|tdT embryos were exposed in utero to a dose of TM (100µg/g of dam body weight) that labels virtually all Sox10⁺ cells within the gut (4). tdT⁺ small intestines were harvested from E13.5 and E15.5 embryos and incubated with Dispase/Collagenase (1 mg/ml, Roche, 296638) at 37°C for 15-30 minutes. The cell suspension was filtered with 40 µm nylon cell strainers (Falcon, 352340) and tdT⁺ cells were isolated using flow cytometry (BD Biosciences Aria Fusion sorter equipped with Diva V8 software and data analysis with FlowJo software). A typical experiment resulted in a yield of 4985±193 tdT⁺ cells at E13.5 (n=3) and 14176±2049 tdT⁺ cells at E15.5 (n=4), indicating a 2.84-fold increase in the number of small intestine ENCCs over this developmental period.

Characterization of ENCC clones during embryogenesis

To identify ENCC clones in E13.5-15.5 SER93|EYFP embryos, guts were fixed in 4% paraformaldehyde (PFA) in PBS (2-6 hours at 4°C) and immunostained as whole-mount preparations with GFP antibodies. Briefly, tissue were permeabilized with 0.3% PBT (PBS with 0.3% Triton-X) for 20 mins, blocked with 10% normal donkey serum in PBT for 2 hours at room temperature and incubated overnight with a rabbit polyclonal GFP antibody (ThermoFisher Scientific, A11122) diluted (1:1000) in blocking buffer. Following several washes with PBT, samples were incubated with Donkey anti-rabbit antibodies conjugated with AlexaFluor488 (ThermoFisher Scientific, A21206, 1:500) for 2 hours at RT. GFP⁺ cell clusters were initially identified by fluorescence stereomicroscopy (Zeiss M2-Bio Stereomicroscope) and analyzed in more detail by laser confocal microscopy (Leica TCS-SP5) using LAS AF software. Images of the entire embryonic gut were generated by merging

independent tiles and processed by Adobe Photoshop CS5.1. For each age, 3-6 independent samples were analyzed. To identify ENCC clones in E13.5-15.5 SER93|Confetti embryos, guts were dissected and fixed in PFA as above. After washing with PBS nGFP⁺, YFP⁺, RFP⁺ and mCFP clusters were identified by fluorescence stereomicroscopy. All clusters were analyzed in detail using a Leica TCS-SP5 confocal microscope equipped with a Nose-dip X20 (1.0 NA) objective. Sequential scans were performed for nGFP (498–510nm), EYFP (521–560nm), RFP (590–650nm) and mCFP (466–495nm). Images were processed using Image J or Adobe Photoshop CS5.1.

Characterization of MADM clusters

To identify MADM clusters, guts were harvested from E12.5-E16.5 and P5 Sox10Cre|MADM and Sox10Cre|MADM-*Ret*^{k-} mice, fixed in PFA for up to 6 hours at 4°C and washed with PBS. The presence of GFP⁺ clusters was initially assessed by fluorescence stereomicroscopy and confirmed by whole-mount immunostaining with GFP antibodies (rat monoclonal, 04404-84, Nacalai Tesque, 1:1000 or rabbit polyclonal, A11122, ThermoFisher Scientific, 1:1000). RFP⁺ clusters were identified by immunostaining with Myc-specific antibody (goat polyclonal, NB600-338, Novus Biologicals, 1:500) (22). Embryonic guts were processed as whole-mount preparations. P5 guts were opened along the mesenteric border, flattened and pinned (mucosa-side down) onto sylgard-coated dishes. 1cm x 1cm squares pieces from longitudinal muscle-myenteric plexus (LM-MP) preparations (4) were immunostained with GFP and myc antibodies. All confocal images were acquired using either a Bio-Rad /Zeiss Radiance 2100 laser confocal scanner (Lasersharpp software), or Leica TCS-SP5 (LAS AF software). Clusters of labelled cells were imaged to a depth of 50µm and optical section thickness ranged from 1-4µm. GFP⁺ and myc (RFP)⁺ clusters were analysed over the entire length of the gut and the total number of labelled cells was obtained. To examine the co-localization of GFP or RFP-Myc signal with lineage-specific markers whole-mount preparations were also stained with HuC/D (mouse monoclonal, A21271, ThermoFisher Scientific, 1:400), BFABP (rabbit polyclonal, Millipore, ABN14, 1:500) or S100β (rabbit polyclonal, Z0311, DakoCytomation, 1:1000) antibodies. Secondary antibodies were used at a dilution of 1:500 in the block buffer and included donkey anti-rat/rabbit/mouse/goat conjugated with AlexaFluors 488, 568, Cy5 or DyLight647 as required (A21206, A10042, ThermoFisher Scientific; 711-175-152, 711-606-152 Jackson ImmunoResearch). Images were processed using Image J and Adobe Photoshop CS5 (Adobe systems).

To examine *Ret* expression in the gut of E16.5 Sox10Cre|MADM-*Ret*^{k-} embryos, following fixation organs were cryo-protected in 30% Sucrose (in PBS) for 24 hours, equilibrated in Sucrose:Gelatin (2:1) solution and snap-frozen in Tissue-Tek O.C.T compound (VWR 361603E). 12-20µm sections were generated using a Microm HM 560 CryoStar cryostat (Thermo Scientific) and thaw-mounted onto SuperFrost Plus (Thermo Scientific) glass microscope slides. The sections were air dried for 2-3 hours at RT and either stored at -80°C for later use or immunostained immediately. For immunostaining cryosections were permeabilized with 0.3% PBT for 10 mins and blocked with 10% normal donkey serum in PBT for 1 hour at room temperature. Sections were incubated overnight with GFP (rat monoclonal, 04404-84, Nacalai Tesque, 1:1000; rabbit polyclonal, A11122, ThermoFisher Scientific, 1:1000) and mouse embryo powder pre-absorbed myc antibodies (goat polyclonal, NB600-338, Novus Biologicals, 1:500) diluted in blocking buffer. Following several washes with PBT, samples were incubated with fluorophore-conjugated secondary antibodies (Donkey anti-rabbit AlexaFluor488, A212106 and Donkey anti-goat AlexaFluor568, A10042, ThermoFisher Scientific, 1:500) for at least 2 hours at RT. After several washes, GFP and RFP stained sections were microwaved in sodium citrate (pH 6.0). Following antigen retrieval, sections were permeabilized with 0.3% PBT and blocked with 10% normal donkey serum in PBT for 1 hour at RT, followed by incubation with the *Ret* antibody overnight at 4°C (goat polyclonal, GT-15002, Immune Systems Ltd., 1:300). Sections were then washed, incubated with biotin-conjugated donkey anti-goat secondary antibody overnight at 4°C (AP180B, Millipore, 1:250), washed again with PBT and incubated with Streptavidin AlexaFluor405-conjugated antibody (S32351, ThermoFisher Scientific, 1:200) at RT for 2 hours. Following several washes, samples were mounted in Vectashield™ without DAPI in order to visualize the immunostained sample in 410-450 nm emission range.

Analysis of ENS clones in adult mice

Guts from 8-12 week old SER93|Confetti mice were washed with PBS, fixed in 4% PFA for a minimum of 4 hours at 4°C and examined for the presence of Confetti clones using a Leica MZ FLIII fluorescence stereoscope equipped with GFP, RFP and CFP filters. The entire monochromatic cluster present on a gut segment was imaged by confocal microscopy with optical sections (2-6µm) spanning a depth of 100µm. For some clones (nGFP⁺/YFP⁺) a depth of 200µm was achieved using the Leica multiphoton (SP5) Mai Tai Ti:Sapphire DeepSee Laser system (Spectra Physics) with a DM6000 microscope assisted by LAS AF software.

Color-coding of sister cells for depth was performed using Image J. To prepare cryosections from gut segments containing a clone, fixed tissue was incubated in PBS-Sucrose for 24 hours, embedded in Sucrose:Gelatin (2:1), mounted onto Tissue-Tek O.C.T compound (VWR) 361603E) and snap-frozen into -60°C isopentane. Cryosections (12 - 20 μ M) were cut using a Microm HM 560 CryoStar cryostat (Thermo Scientific) and thaw-mounted onto SuperFrost Plus (Thermo Scientific) microscope slides. Sections were air dried for 2-3 hours at RT and then either stored at -80°C for later use or processed immediately for immunostaining. For certain ENS clones, their myenteric and submucosal components were imaged separately by dissecting the longitudinal muscle-myenteric plexus (LM-MP) and circular muscle-submucosal plexus (CM-SMP) layers from fresh gut tissue. These preparations were then fixed in ice-cold 4% PFA for 2-6 hours at 4°C and washed with PBS prior to further processing. For immunostaining of whole gut pieces, tissue was permeabilized with 0.3% PBT for 30 mins and then blocked with 10% normal donkey serum in PBT for 2 hours at room temperature (RT). Samples were incubated overnight with primary antibodies: HuC/D (mouse monoclonal, A21271, ThermoFisher Scientific, 1:400), PGP9.5 (rabbit polyclonal, 7863-0504, Biogenesis, 1:1000), S100 β (rabbit polyclonal, Z0311, DakoCytomation, 1:1000), Sox10 (goat polyclonal, sc-17343, Santa Cruz, 1:200), CALR (goat polyclonal, Swant, CG1, 1:500), nNOS (rabbit polyclonal, 617000, Zymed, 1:400; Sheep polyclonal, gift from Dr. Furness, 1:1000), Neurofilament-M (rabbit polyclonal, Millipore, AB1987, 1:300), ChAT (goat polyclonal, Millipore, AB144P, 1:200) diluted in blocking buffer. Following washes with PBT, species-specific AlexaFluor647-conjugated secondary antibodies (Donkey anti-mouse, 715-605-151; Donkey anti-rabbit, 711-605-152; Donkey anti-goat, 705-605-003; Jackson ImmunoResearch, 1:500) were applied to the samples for 2-4 hours at RT. The same antibodies were also used for immunostaining of gut sections as described above.

Quantification and Statistical Analysis

Data have been obtained from a minimum of three independent experiments. Numbers of replicates (n) are provided in the text or figure legends. Data are mainly presented as mean \pm standard error of the mean (SEM) unless otherwise mentioned. All error bars represent SEM. Statistical analysis was performed with GraphPad Prism 6 (GraphPad Software) and Microsoft Excel 9 (Microsoft). Significant differences between data sets have been obtained with different tests as mentioned mostly in the figure legends.

Single-cell RNA sequencing

SER93|tdT embryos were exposed to TM at E12.0 in utero (100µg/gr of dam body weight) and harvested 24 hours later. Individual small intestines were digested with Dispase/Collagenase (1 mg/ml, Roche, 296638) at 37°C for 15 minutes and manually triturated to obtain a single-cell suspension. tdT⁺ cells were separated using the Aria Fusion cell sorter (BD Biosciences) with the 100µm nozzle at 26psi and collected in 2% FBS in OptiMEM (Life Technologies). Dead cells were excluded with a cell viability dye (Zombie Aqua, BioLegend) that was added to the single cell suspension (2 ng/ml). The Fluidigm C1 automated microfluidic system was used to randomly capture 192 individual cells into 5-10µm chips. The SMARTer Ultralow RNA kit (Clontech #634833) was used to reverse transcribe poly (A) RNA and amplify cDNA. ERCC spike-ins (Life Technologies #4456740) were added at a dilution of 1:80000. cDNA concentration of each cell sample was quantified using the Promega Quantifluor dsDNA on Glomax system and quality of random samples was checked on high-sensitivity DNA chip on Agilent Bioanalyser 2100. Amplified cDNA (0.125-0.375 ng) was used for sequencing libraries with the Illumina Nextera XT DNA kit (Illumina #FC-131-1096). All libraries were sequenced as paired-end 76 using the Illumina HiSeq4000 system. Single cell RNA-Seq data of two independent experiments comprising 80 and 72 cells were obtained as paired-end reads. Cell samples contained typically 4-6 million reads. Sampled sequences were aligned to the *Ensembl GRCm38* genome using *Tophat2* (29); alignment rates were typically 80-90%. Transcript counts were obtained using the *featureCounts* program (30). Further processing of transcript counts was performed in the R environment (31). Transcript counts of all samples were merged into a single matrix and passed through a quality filter, where cells with total read counts below 10⁵ were removed as well as genes with no counts in any cell sample. The dimension of the final data matrix was 20307 genes by 144 cells. The entire RNA-Seq data flow was managed by a *GNU make* pipeline. Transcript counts were further analysed using the *scLVM* package (32). After normalisation, correction for technical noise and transformation to log₁₀ scale, only heterogeneously expressed genes were selected (9628 genes, False Discovery Rate < 0.1) as well as cells with a combined neuronal and glial marker gene expression above 10³ (120 cells). Data analysis and plots were based on this final matrix of 9628 genes and 120 cells.

Linear regression and ANOVA

Gene correlation was evaluated through a combination of linear regression and ANOVA. The transcript counts of all variable genes were regressed against those of a linear combination of

the marker genes *Fabp7*, *Plp1*, *Tubb3*, *Phox2b* and *Ret*. Because of the high correlation of *ErbB3* and *Sox10* with *Fabp7* and of *Elavl4* with *Tubb3*, these marker genes were excluded from the regression model to avoid redundancy. ANOVA of the regression results was performed to assess the significance of the fits. Lists of correlated genes were extracted for the marker genes by applying cut-offs to the regression coefficient (> 0.4) and the p-value ($10^{-5.3}$: 5% error rate with Bonferroni correction). The 35 genes with the highest correlation to the marker gene are shown.

Plot computations:

Biplot: Transcript counts were corrected for cell cycle effects (Gene Ontology term GO:0007049) by assigning the associated variance to a latent factor. Dimensionality reduction of the expression variance between single cells was performed using Principal Component Analysis (PCA). Projection of the cells onto the plane of first two principal components (PC1 and PC2) and colour coding by the expression gradient of marker genes (*Tubb3*, *Elavl4*, *Phox2b*, *Ret*, *ErbB3*, *Sox10*, *Plp1* and *Fabp7*) showed that a main component of the variance observed is reflected in the distribution of these markers.

Heatmap: The heatmap of marker genes was created using the WPGMA agglomerative hierarchical clustering method and the default Euclidean distance matrix of the shown neuronal and glial marker genes. The colour code is black, grey, yellow and white in increasing order of gene expression. The color bar on the (horizontal) cell axis illustrates the expression gradient of neuronal (orange) and glial (blue) marker genes. The heatmap of marker genes combined with 100 random (heterogeneously expressed) genes was created using 'complete' agglomeration and a '1 - correlation' distance matrix.

Perspective plot: The perspective plot of single cells was computed using the 'kde2d' two-dimensional kernel density estimator given the single cell distribution within the xy-plane of neuronal (orange) and glial (blue) marker expression.

Calcium imaging and analysis

The entire gastrointestinal tract from adult SER93|Confetti mice and wild type C57BL/6N mice was dissected out and pinned flat in a Sylgard-lined dish filled with Krebs solution (bubbled with 95% O₂ - 5% CO₂, RT). Given the spectral properties of Fluo-4, our experiments focused on RFP⁺ clones. Intestinal segments from SER93|Confetti mice containing RFP⁺ clusters were identified using a Leica MZ FLIII fluorescence stereomicroscope. The mucosal, submucosal and circular muscle layers were carefully removed to obtain a longitudinal muscle-myenteric plexus (LM-MP) preparation containing

the clone which was then mounted over a small inox ring, immobilized by a matched rubber O-ring and loaded with 2 μ M Fluo-4 AM (Life Technologies; RT 30 min) in Krebs with Kolliphor[®] EL (0.01%, Sigma). LM-MP preparations were placed in a recording chamber and constantly superfused with Krebs solution (RT) containing nifedipine (1 μ M, Sigma). Imaging of LM-MP preparations from SER93|Confetti mice was performed on an upright Olympus BX61WI confocal microscope controlled by Olympus Fluoview (FV10-ASW ver. 4) software. Changes in Fluo-4 fluorescence were recorded at 1-2 Hz through an Olympus X20 (NA 0.50) objective, with 488 nm Argon laser excitation, and 500–545 nm spectral detector emission collection. RFP was excited with a diode-pumped solid-state (DPSS) laser at 559 nm, and fluorescence emission collected at 570–670 nm. The sister neurons analysed belonged to 1 (33%), 2 (58%) or 3 (9%) enteric ganglia and 112 non-labelled neurons were used as clonally unrelated cells. Myenteric neurons were identified by depolarization (75 mM K^+) and by electrical stimulation using a train (20 Hz, 2 s) of pulses (300 μ s) transmitted via a focal electrode (50 μ m diameter platinum wire) placed on an interganglionic fiber tract adjacent to the imaging area. The vast majority of Fluo-4-loaded RFP⁺ neurons (43/45, 8 clones from 6 mice), displayed significant increases in intracellular $[Ca^{2+}]$ in response to depolarization by 75mM K^+ or trains of electrical pulses. No significant difference was detected between RFP⁺ and RFP⁻ neurons regarding baseline intracellular $[Ca^{2+}]$ or Ca^{2+} transient amplitude evoked by electric pulse trains (Fig. 5, D and E). For the pairwise analysis prominent Ca^{2+} transients were evoked in differential sets of neurons within the field of view by single electrical pulses conveyed to 3 independent interganglionic nerve strands that were linked to the ganglia harbouring the identified RFP⁺ neurons (Fig. 5, A to C).

The contribution of synaptic communication was examined by analysing neuronal responses to single-pulse electrical stimulation in the presence of hexamethonium, an inhibitor of nicotinic synaptic neurotransmission. LM-MP preparations obtained from C57BL/6N mice were recorded on an upright Zeiss Axio Examiner.Z1 microscope equipped with a Poly V xenon monochromator (TILL Photonics) and water dipping lens (X20, 1.0 NA, Zeiss). Fluo-4 was excited at 475 nm and captured at 525/50 nm (at 2 Hz) on a Sensicam-QE CCD camera (PCO) using TillVisION (TILL Photonics). Each preparation was stimulated electrically (single pulse) two times, 10 min apart: first in control conditions and then again in the presence of hexamethonium (200 μ M, Sigma) following a 10 min wash-in. Analysis was performed with custom-written routines in Igor Pro (Wavemetrics) (33). Regions of interest were drawn, after which average Ca^{2+} signal intensity was calculated, normalized to the initial Fluo-4 values and reported as F_i/F_0 . Cells were considered as responders when the

Fluo-4 signal rose above baseline plus 3 times the intrinsic noise (standard deviation) during the recording. The amplitudes of Ca^{2+} transients were measured as the maximum increase in $[\text{Ca}^{2+}]_i$ above baseline ($\Delta F_i/F_o$).

Supplementary Figure Legends

Figure S1. Generation of ENS clones.

(A, B) Whole-mount preparations of gut from E13.5 SER93|EYFP embryos exposed to tamoxifen. The indicated doses refer to μg of tamoxifen per g of dam body weight. The partial colonization of the colon by ENCCs is evident in A (arrow). Insets 1, 2 and 3 in B show magnifications of YFP⁺ cells indicated by the corresponding arrows. Scale bars: main panels, 500 μm ; insets: 10 μm . (C) Timeline of ENS clone induction and analysis in SER93|EYFP and SER93|Confetti mouse embryos. Tamoxifen was administered intraperitoneally to the dam at E12.5 (red arrow) and clones were analyzed 24, 48 or 72 hours later (green arrows). (D) The average number of YFP⁺ clusters in the gut of tamoxifen-treated SER93|EYFP embryos (black bars) was similar across the three stages analyzed (E13.5-15.5). In contrast, the average size of YFP⁺ clusters (orange bars) increased during this period (Tukey's multiple comparison test: E13.5 Vs E14.5: Not significant $p=0.12$; E13.5 Vs E15.5 **** p value <0.0001 ; E14.5 Vs E15.5 Not significant, $p=0.37$). (E) Distribution of ENS cluster size in the gut of SER93|EYFP embryos at E13.5 (blue bars), E14.5 (brown bars) and E15.5 (green bars). (F) Examples of YFP⁺ clusters identified by GFP immunostaining in the gut of E13.5-15.5 SER93|EYFP embryos. Scale bars: 50 μm . (G) Sparse labelling of ENCCs in the gut of E13.5 SER93|Confetti embryos exposed to tamoxifen at E12.5. Insets show zoomed-in images of the RFP⁺ and mCFP⁺ clusters. Scale bar: main panel 500 μm . (H) The average number of Confetti⁺ clusters in the gut of tamoxifen-treated SER93|Confetti embryos (black bars) is similar across all stages analysed (E13.5-15.5). In contrast, the average size of Confetti⁺ clusters (orange bars) increased during this period (Tukey's multiple comparison test: E13.5 Vs E14.5 ** p value = 0.0064; E13.5 Vs E15.5 **** p value <0.0001 ; E14.5 Vs E15.5 *** p value = 0.0001). (I) Distribution of ENS cluster size in the gut of SER93|Confetti embryos at E13.5 (blue bars), E14.5 (brown bars) and E15.5 (green bars). (J) Examples of monochromatic clusters in the gut of TM-treated SER93|Confetti embryos at E13.5-15.5. Scale bars: 10 μm (for the CFP⁺ cells) and 20 μm (for the RFP⁺ and YFP⁺ cells). (K) Distribution of labelled ENCC clusters along the gut of SER93|EYFP and SER93|Confetti mice at the indicated stages. "Embryonic" refers to the cumulative distribution observed at the three embryonic stages analyzed. Data is presented as mean \pm SEM. (L) Quantification of Confetti⁺ clusters observed in the gut of SER93|Confetti embryos and adult mice. Data is presented as mean \pm SEM.

Figure S2. Lineages and Subtypes in an adult NG clone.

(A-D) Cryosections from an RFP⁺ NG clone (shown in the first column of panels) were immunostained for a pan-neuronal (PGP9.5 in A), a pan-glial (S100 β in B), and two neuronal subtypes (ChAT in C and nNOS in D) markers (second column of panels). The third column shows the sections labelled with Dapi and the fourth column shows the merged images. LP, lamina propria; SMP, submucosal plexus; MP, myenteric plexus. Scale bar: 20 μ m.

Figure S3. Commitment of ENCCs to the neurogenic or gliogenic lineage precedes acquisition of subtype identity.

(A) An RFP⁺ NG clone immunostained for the neuronal subtype markers nNOS (neuron indicated by arrow 1 is shown in detail in inset 1a-c), CALR (inset 2a-c), NF-M (inset 3a-c) and ChAT (inset 4a-c). Neurons expressing each of these markers were present in this clone. (B) A CFP⁺ G clone immunostained for the glial marker S100 β . Insets 1a-b, 2a-b, 3a-b and 4a-b, show magnifications of the cells indicated by arrow 1, 2, 3 and 4, respectively. Cyan represents CFP signal and white represents S100 β signal. Cyan arrows in 1b, 2b, 3b and 4b indicate the mCFP⁺ cells shown in 1a, 2a, 3a and 4a. All morphological subtypes of enteric glia were present in this clone. (C) A 10-neuron RFP⁺ N clone immunostained for the neuronal subtype markers CALR and nNOS. Insets 1a-d, 2a-d and 3a-d show magnifications of neurons indicated by arrows 1, 2 and 3, respectively. Neuron 1 is CALR⁺nNOS⁻, neuron 2 is CALR⁻nNOS⁺ and neuron 3 is CALR⁻nNOS⁻. (D) A 4-neuron YFP⁺ N clone immunostained for CALR and NOS. Insets 1a-d, 2a-d, 3a-d and 4a-d show magnifications of neurons indicated by arrows 1, 2, 3 and 4, respectively. All 4 neurons were CALR⁺nNOS⁻. Scale bars: main panels, 500 μ m, insets, 10 μ m.

Figure S4. Mosaic analysis of ENS development and *Ret* mutagenesis using MADM.

(A) Schematic representation of Sox10Cre|MADM (top panel) and Sox10Cre|MADM-*Ret*^{k-} (bottom panel) modified from (22). In Sox10Cre|MADM, Cre-induced G2 recombination followed by X segregation (G2-X) results in a GFP⁺ (green) and myc(RFP)⁺ (red) daughter cells while G1/G0 or G2 recombination followed by Z-segregation (G2-Z) results in either unlabelled (white) or double labelled (yellow) daughter cells. In Sox10Cre|MADM-*Ret*^{k-}, the *Ret*^{k-} allele was linked by meiotic recombination to the MADM-GR cassette in the *Rosa26* locus. G2-X recombination results in GFP⁺ *Ret*^{k-} homozygous (green) and myc(RFP)⁺ (red) wild-type cells. G0/G1 and G2-Z recombination results in either unlabelled (white) or double labelled (yellow) *Ret*^{k-} heterozygous cells. (B) Ret immunostaining on cryosections from the gut of E16.5 MADM embryos. Top panels show a GFP⁺RFP⁻Ret⁺ cell from the gut of a

Sox10Cre|MADM embryo. Middle panels show a GFP⁺RFP⁺Ret⁺ from the gut of a Sox10Cre|MADM-Ret^{k-} embryo. Lower panels show a GFP⁺RFP⁻Ret⁻ cell from the gut of a Sox10Cre|MADM-Ret^{k-} embryo. +/+, +/- and -/- refer to the genotype of the indicated cells at the *Ret* locus. Scale bar: 10 μ m. (C) Representative images of whole-mount gut preparations from the gut of E16.5 Sox10Cre|MADM animals immunostained with the neuronal marker HuC/D. Both the GFP⁺ and the RFP⁺ cells in the E16.5 gut are HuC/D⁺. The strong GFP signal allows clear visualization of neuronal projections (arrows) which independently confirms the neuronal identity of the GFP⁺ cell. Scale bar: 20 μ m. (D) Image from a whole-mount gut preparation from the gut of E16.5 Sox10Cre|MADM-Ret^{k-} animal immunostained with the neuronal marker HuC/D. One of the RFP⁺ cells is HuC/D⁺ but all GFP⁺ cells are HuC/D⁻. Also, none of the GFP⁺ cells carry neuronal projections. Scale bar: 20 μ m. (E) Bar chart showing the ratio of the total number of GFP⁺ and RFP⁺ cells in the gut of Sox10Cre|MADM (black) and Sox10Cre|MADM-Ret^{k-} (orange) animals at E16.5 and P5. The presented ratios are based on the following absolute numbers of cells. Sox10Cre|MADM: E16.5 GFP⁺=816, RFP⁺=758, n=67 guts; P5 GFP⁺=173, RFP⁺=160, n=10 guts. Sox10Cre|MADM-Ret^{k-}: E16.5 GFP⁺=1994, RFP⁺=1276, n=97 guts; P5 GFP⁺=472, RFP⁺=198, n=10 guts. Two-tailed Student's t test, Mann-Whitney U post-hoc, ****: p<0.0001; NS: p=0.11; ***p=0.001. (F) Percentage of neurons within the RFP⁺ (red bars) and GFP⁺ (green bars) cell population, at E16.5 and P5. Absolute numbers are indicated. Wilcoxon signed rank test; *** p value=0.0002.

Figure S5. Spread of ENS clones depends on proliferation-driven local cell interactions. (A) Example of a nGFP⁺ clone to demonstrate that surface area is defined by a convex envelope that runs along the perimeter cells of a cluster. Scale bar: 200 μ m. (B) Scatterplots of clone size and surface area of N (blue), G (red) and NG (green) ENS clones. (C) Proliferation-driven spread of clones generated from founder cells undergoing 1 to 7 cell divisions simulated with an agent-based model. Clones grow either within a background of proliferative unlabelled cells which undergo 7 cell divisions (red circles) or in isolation (black circles). AU: arbitrary units. (D) Agent-based model simulations of the spread of clones generated from founder cells that divide amongst unlabelled cells proliferating at the same rate (red circles), undergoing fewer (half) cell divisions (dark blue circles) or having longer (2x) cell cycle (light blue circles). Black circles show the spread of clones growing in isolation. Solid lines show that simulated spreads are consistent with theoretical spreads of homogenously mixed clones described in Equation (S4) (Supplementary material). The

difference in the founder proliferation potential with respect to unlabelled cells results in type N clones subjected to higher frequency of spatial interactions and reaching larger spreads than type G and NG clones with similar number of cells; **(E)** Comparison between observed (circles) and predicted (solid lines) surface area of N (blue), G (red) and NG (green) clones. Circles represent the same values shown in panel B. Predicted values were estimated independently of observations (model not fitted to the data) assuming that spread of clones depends on the proliferation potential of the founder cell, proliferation-driven cell interactions and growth of the intestine as described in Equation (S7) (Supplementary material). Broken lines show the predicted values of spread assuming no intestinal growth (Equation (7) reduces to Equation (4)). **(F)** Agent-based model simulation of clonal spread in the case of a large (95 cells; 'a', 'c') or a small (14 cells; 'b', 'd') clone. 'a' and 'b' clones (red cells) intermingle with non-labelled cells (grey), 'c' and 'd' clones grow in isolation. Non-labelled cells have the same proliferation potential to clone 'a' but undergo twice as many cell divisions relative to clone 'b'. Although clone 'a' is approximately 6.8 times larger relative to 'b', their spread (shadowed) areas do not reflect that difference (640 and 415 AUs, respectively). In contrast, when clones grow in isolation, their corresponding surface areas are 99 and 16 AUs, respectively, reflecting their difference in number of cells. **(G)** Simulated overlapping clones (red and yellow cells) generated from nearby founder cells.

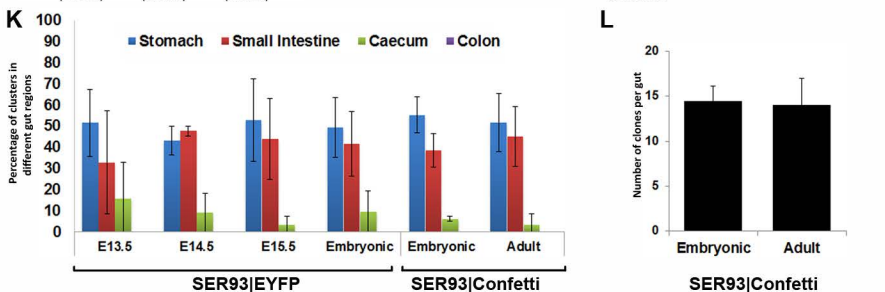
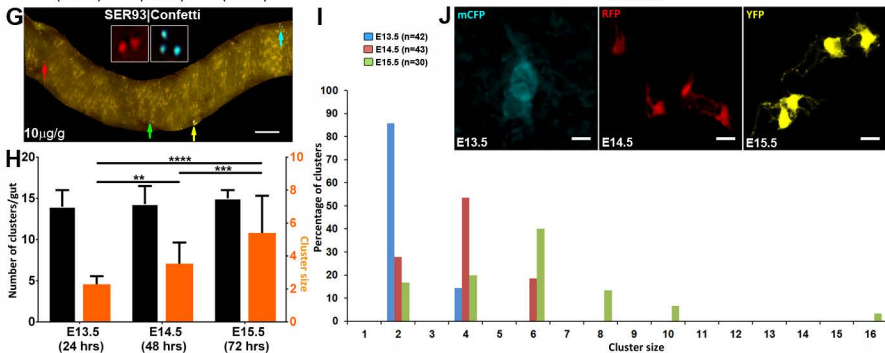
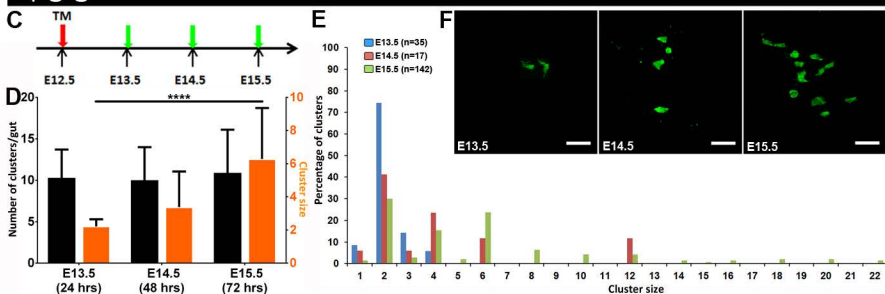
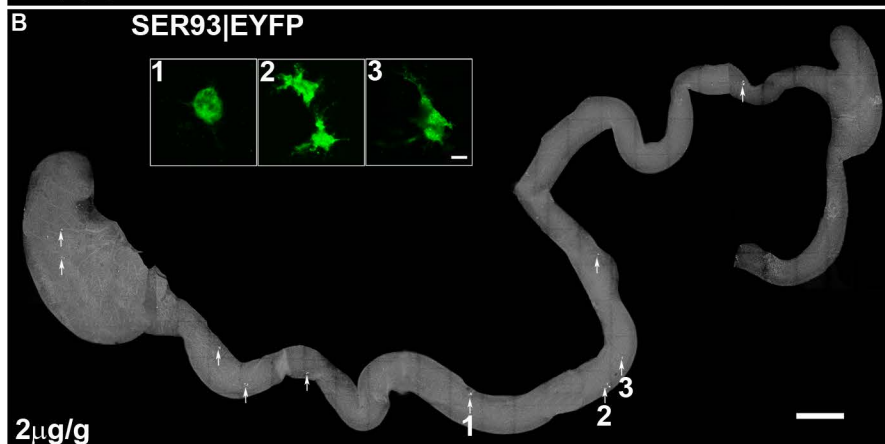
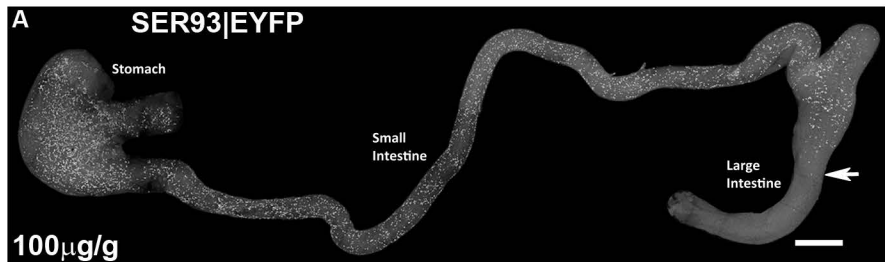
Figure S6. Model depicting the development of ENS layers.

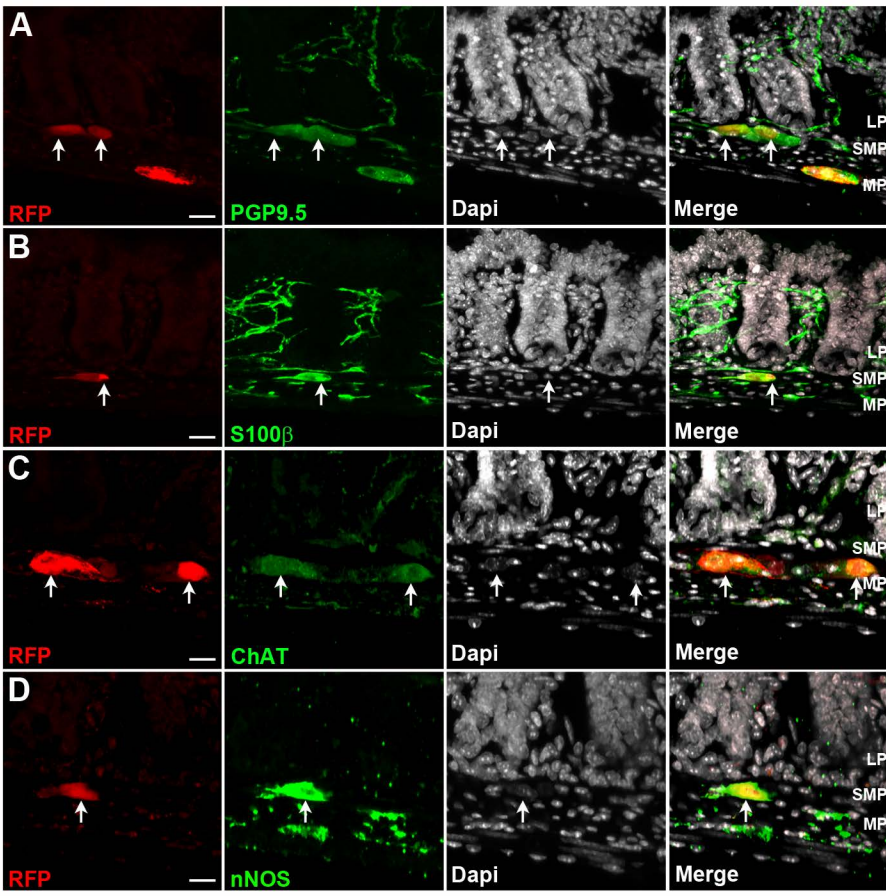
ENCCs colonize the longitudinal axis of the small intestine by migrating within its outer wall (plane of the future myenteric plexus-MP). Upon completion of rostro-caudal migration, NG progenitors give rise to neurogenic (N) and gliogenic (G) cell precursors. N cells and derivative neurons are restricted to the myenteric plexus. In contrast NG, G cells are capable of migrating along the serosa-lumen axis to colonize the future submucosal plexus (SMP) where NG cells generate submucosa-specific N cells and neurons. Cells of the glial lineage can eventually migrate further into the mucosa.

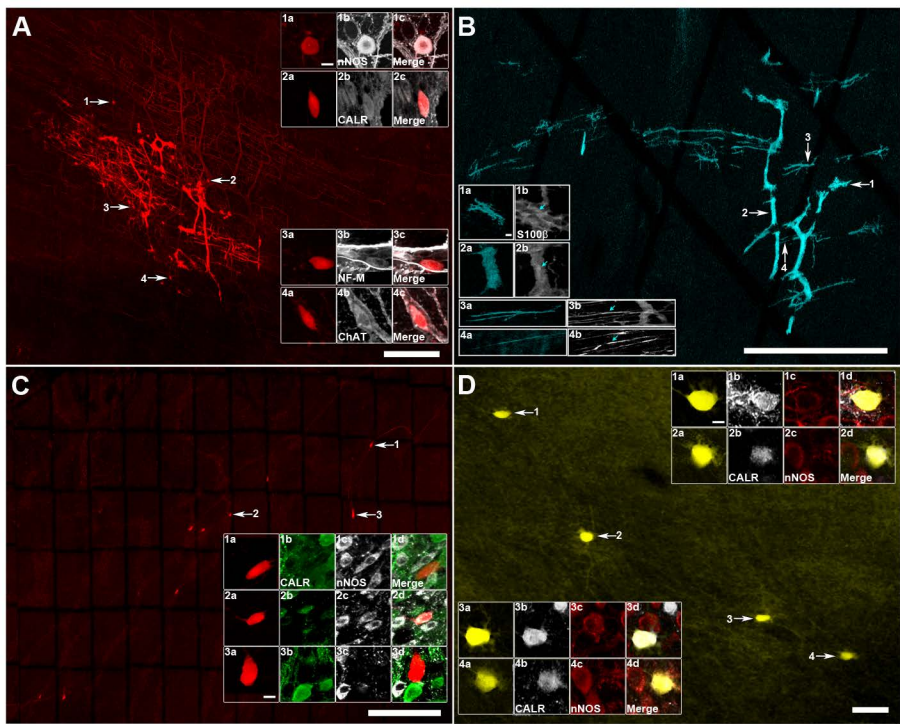
Figure S7. Activity of lineage-related neurons

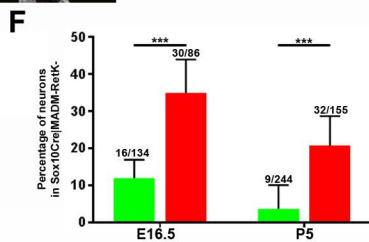
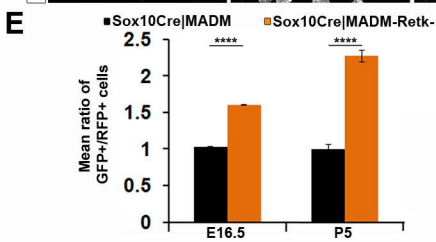
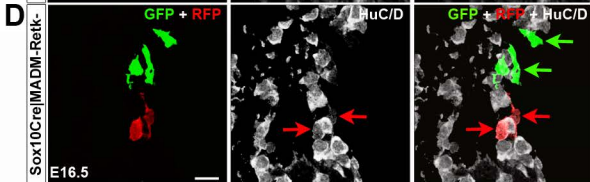
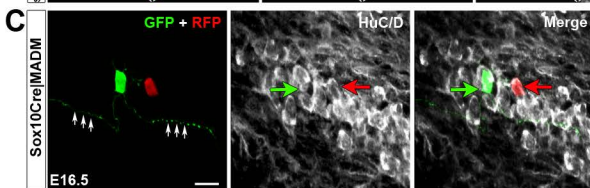
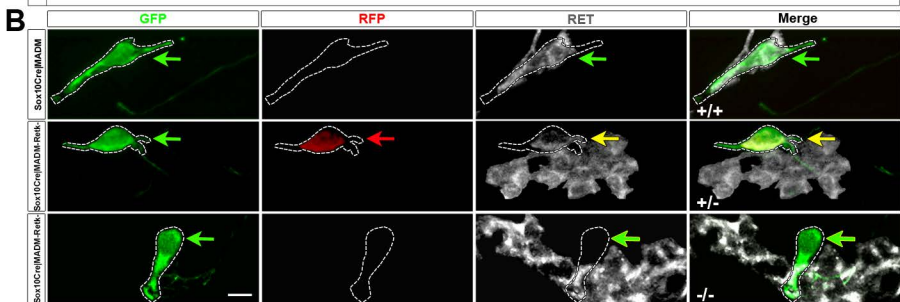
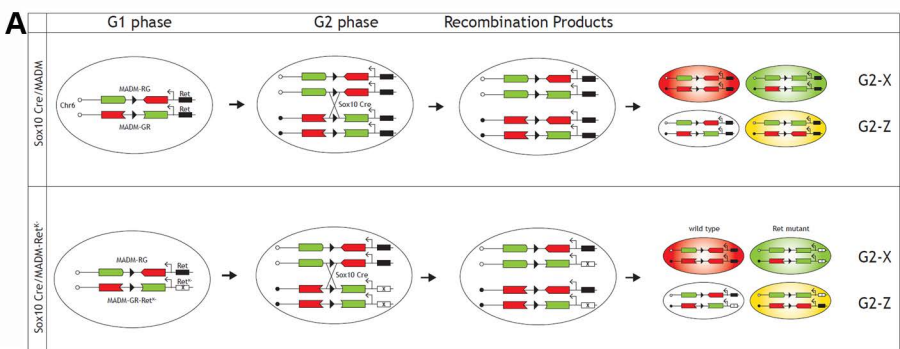
(A) SER93|Confetti myenteric plexus preparation containing three RFP-positive sister neurons (red) from an NG clone loaded with the fluorescent Ca^{2+} indicator Fluo-4 (green). Images show fluorescence at baseline (upper panels) and upon 75mM K^{+} depolarization (lower panels; Cells displaying a Ca^{2+} transient are falsely-coloured in green by an activity over time operation, AoT). The average (\pm SEM) Fluo-4 traces upon 75mM K^{+} stimulation

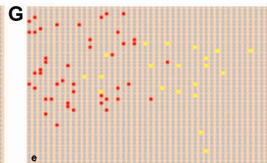
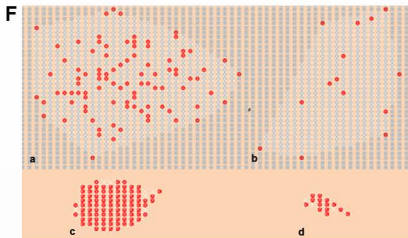
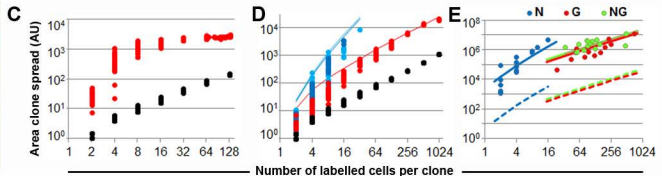
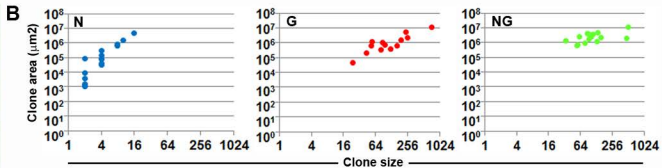
of the RFP-positive (red) and non-labelled (black) neurons present within the field of view are shown in the lower left panel. Scale bar: 100 μm . **(B)** Representative images of a ganglion within a longitudinal muscle-myenteric plexus preparation from C57Bl/6 mice loaded with the fluorescent Ca^{2+} indicator Fluo-4 (grey values) at baseline (top left) and during a train of electrical pulses (300 μs , 20 Hz, 2s) (top right). The asterisk shows the location of the stimulating electrode. Lower images show the same ganglion with cells displaying a Ca^{2+} transient (active pixels are falsely-coloured by an activity over time operation, AoT) upon a single electrical pulse in control conditions (green) and under superfusion with hexamethonium (hex, red). Arrowheads point to 2 neurons responding in both conditions. Arrows point to 2 neurons that do not respond when nicotinic acetylcholine receptors are blocked by hexamethonium. Left graph: Quantification of the proportion of neurons responding to a single electrical pulse in control and hexamethonium condition (Two-tailed Student's t test, ns: $p > 0.05$). Right graph: The maximal amplitude of the Ca^{2+} transients upon single pulse stimulation of neurons responding in both conditions (Paired t test, *: $p < 0.05$).

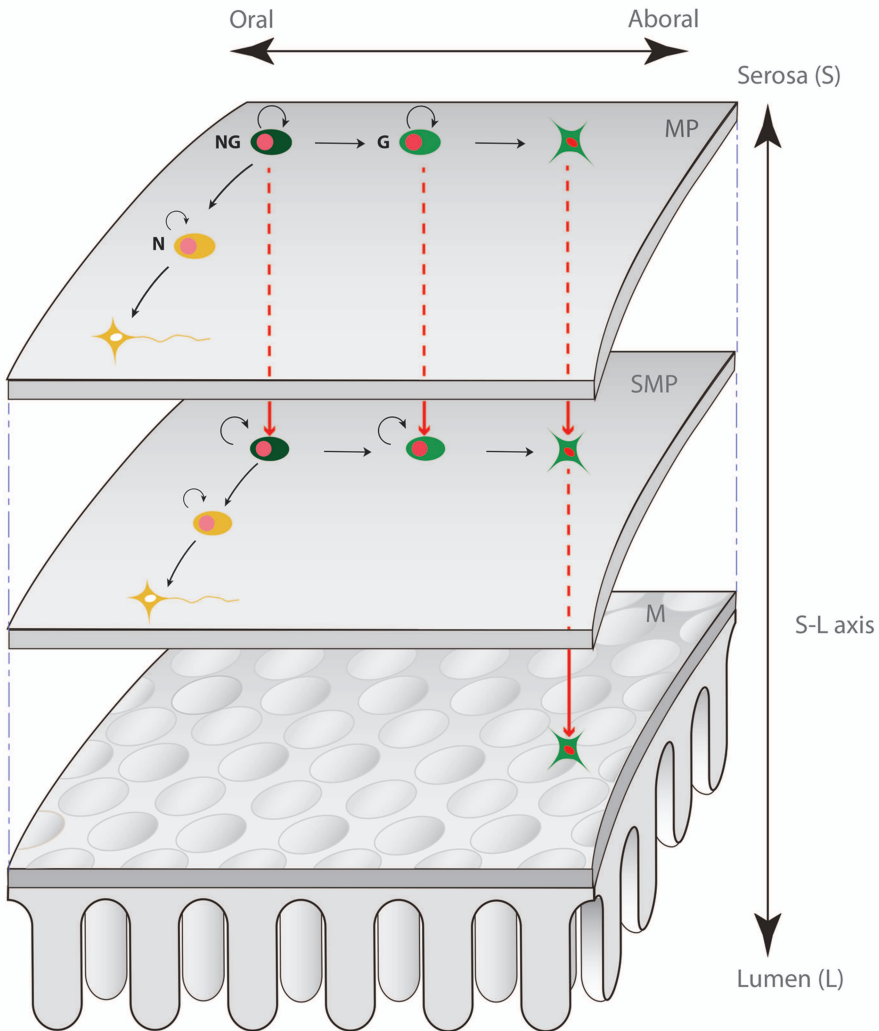


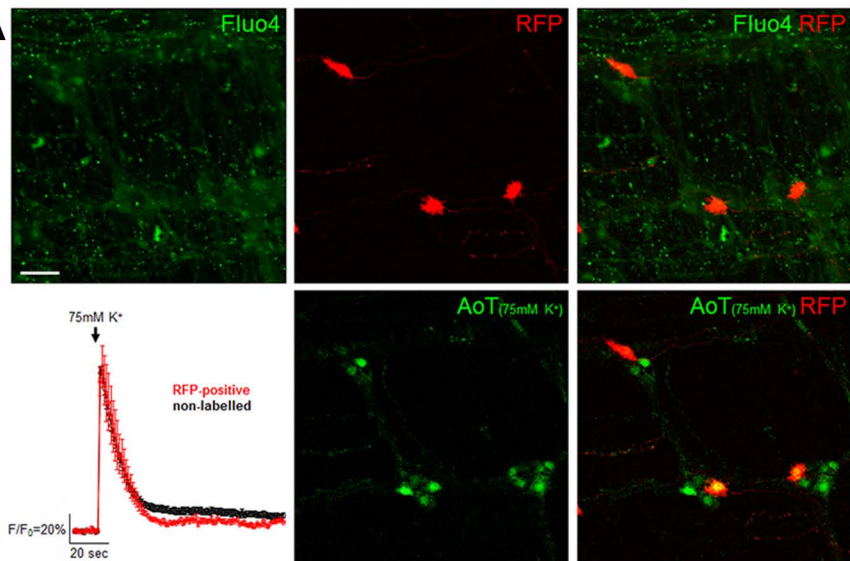
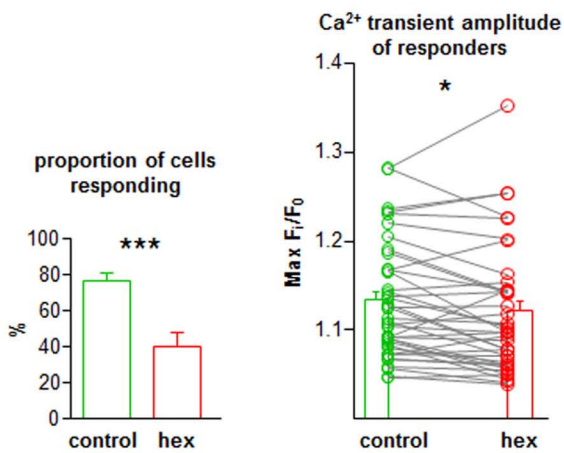
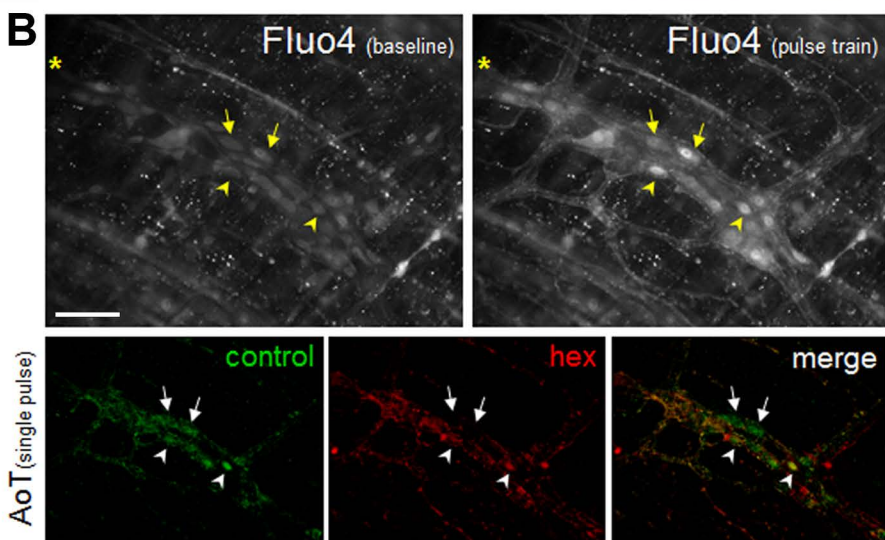










A**B**

Supplementary Table 1

Clone No	Clone Size	CALR	nNOS	NF-M
1	2	-	-	Nor Tested (NT)
2	2	-	-	NT
3	2	-	-	NT
4	2	-	2+	NT
5	2	2+	-	NT
6	2	2+	-	NT
7	2	-	-	NT
8	2	-	NT	-
9	2	2+	NT	-
10	2	2+	NT	-
11	2	2+	NT	-
12	2	-	NT	-
13	4	-	-	NT
14	4	4+	-	NT
15	4	-	NT	4+
16	4	-	NT	-
17	4	4+	NT	-
18	4	4+	NT	-
19	4	4+	NT	-
20	4	4+	NT	-
21	4	NT	-	4+
22	8	2+	6+	NT
23	8	2+	2+	NT
24	8	-	4+	NT
25	10	4+	2+	NT
26	16	-	2+	NT

Supplementary Table 2

Allele	Primers
<i>Sox10</i> -CreERT2 (SER93 and SER26)	5' GAG GGA CTA CCT CCT GTA CC 3' 5' TGC CCA GAG TCA TCC TTG GC 3'
<i>Rosa26R</i> -EYFP (R26R-EYFP)	5' GCTCTGAGTTGTTATCAGTAAGG 3' 5' GGAGCGGGAGAAATGGATATG 3' 5' GCGAAGAGTTTGTCTCAACC 3'
<i>Rosa26R</i> -Confetti (R26R-Confetti)	5' GAA TTA TTC CGG TAT AAC TTC G 3' 5' AGA GTA TAA AAC TCG GGT GAG C 3'
<i>Rosa26R</i> -CAG-iL4 (R26R-Tomato)	5' AAG GGA GCT GCA GTG GAG TA 3' 5' CCG AAA ATC TGT GGG AAG TC 3' 5' CTG TTC CTG TAC GGC ATG G 3' 5' GGC ATT AAA GCA GCG TAT CC 3'
<i>Rosa26R</i> -MADM6 (GR and RG)	5' CTC TGC TGC CTC CTG GCT TCT 3' 5' TCA ATG GGC GGG GGT CGT T 3' 5' CGA GGC GGA TCA CAA GCA ATA 3'
<i>Ret</i> K	5' TGG GAG AAG GCG AGT TTG GAA A 3' 5' TTC AGG AAC ACT GGC TAC CAT G 3' 5' AGA GGC TAT TCG GCT ATG ACT G 3' 5' CCT GAT CGA CAA GAC CGG CTT C 3'

Movie Captions

Movie 1. Agent-based model simulation of the expansion of a clone from 1 to 95 labelled (red) cells intermingling with proliferative non-labelled cells (grey cells) with the same proliferation potential.

Movie 2. Agent-based model simulation of the expansion of a clone from 1 to 14 labelled (red) cells intermingling with non-labelled cells (grey cells) proliferating at higher (1.7 fold) rate.

Movie 3. Agent-based model simulation of the expansion of a clone from 1 to 8 labelled (red) cells intermingling with proliferative non-labelled cells (grey cells) proliferating at higher (2.2 fold) rate.

Movie 4. Agent-based model simulation of the expansion and overlapping of clones (red and yellow cells) generated from nearby founder cells.

Computational and analytical models for ENS clone expansion

Agent-based model to simulate proliferation-driven short-range ENS cell interactions during development

We developed an agent-based model to simulate proliferation-driven local cell interactions of ENS cells during development. The agents are individual cells located on a discrete lattice and characterized by their coordinates, rate of cell division and labelled or unlabelled state. Following the division of a parent cell (labelled or unlabelled) daughters can occupy one of eight neighbouring positions with equal probability. If the location is already occupied, the resident cell is displaced and in turn it displaces one of its neighbours creating a chain of steps equivalent to a random walk in 2 dimensions (2D) which stops when a non-occupied position is reached. It can be proven that this model results in clone cells homogeneously mixed with unlabelled cells. The model is simulated with a Monte Carlo algorithm which executes iteratively the sequence of events with the shortest waiting time and it is implemented in Visual Basic. The number of cells within a clone and their spread (estimated as the area included within a convex envelope) were recorded during simulations, which were repeated 30-50 times. The duration of the division cycle was assumed to have a gamma distribution with expected value equal to 17 arbitrary time units (and standard deviation equal to 1.7 units), which is based on the reported 17 h duration of cell cycle for ENCCs (1 arbitrary time unit = 1 h) (34). To initiate simulations with non-synchronized cell populations, the first division time of each cell was chosen randomly along the cell cycle. The area of a cell was equal to $\sigma = 1$ arbitrary unit (AU). We used a complete 2D lattice (no gaps) in which the chain of displacements initiated by a cell division stopped when they reached an empty position at the edge of the lattice. Simulations were initiated with a labelled cell at the centre of a 5x5 lattice which was extended if necessary to separate labelled cells from the edges by at least 2 cell rows. The performance of the computational model was evaluated by comparing the spread of simulated clones with the theoretical spread of clones growing among unlabelled cells, as estimated in the next section.

Analytical model to describe the area of spread as a function of cell proliferation and gut expansion.

The spread of the clone depends on the proliferation potential of the founder cell (experimental data), random short-range proliferation-driven interactions between clonal and

non-labelled cells (computational model) and is likely to be influenced by the growth of the intestine during development. According to the agent-based model, proliferation-driven local cell interactions take place at random and result in homogenous mixing of clonal and non-labelled cells. Then the number of labelled cells per spatial unit in a homogenous mixture of clonal and unlabelled cells follows a Poisson distribution. This allows the estimation of the theoretical distributions of the maximum clone spread lengths in orthogonal directions (principal axes) and of the spread area as described below.

Assuming $X > 1$ labelled cells are homogeneously mixed with a number, greater than 0, of non-labelled cells per spatial unit. Thus, X has a Poisson distribution. Consider L_1, L_2, \dots, L_X to be the projections of X labelled cells on the first principal axis of the area of spread of the total population, whose projections are spread on a length equal to L . Let L_1, L_2, \dots, L_X be ordered from smallest to largest and shifted so that L_1 has a value equal to 0 as starting reference point and with the maximum length $L_X \leq L$. It can be demonstrated that the conditional joint density of (L_2, \dots, L_X) , has a density function equal to

$$f(L_2, \dots, L_X) = \frac{(X-1)!}{u^{X-1}} \quad \text{if } L_1 \leq L_2 \leq \dots \leq L_X \leq u. \quad (\text{S1})$$

From Equation (S1) it is possible to derive the marginal density L_X , which is the maximum distance between any pair of cells along the direction of the first principal axis, as

$$f_{L_X}(u) = \frac{(X-1)!}{(X-2)!} \frac{u^{X-2}}{L^{X-1}} \quad 0 \leq u \leq L, \quad (\text{S2})$$

and its expected value as:

$$E[L_X] = \frac{(X-1)L}{X}. \quad (\text{S3})$$

Equation (S3) expresses the maximum length of the spread of a labelled clone with X cells, L_X , homogeneously mixed with non-labelled cells. The maximum length of the spread of the total cell mixture is equal to L . A parallel analysis on the second principal axis direction, which is orthogonal to the first principal axis, concludes that the expected maximum length of spread of the labelled clone on this axis, $E[W_X]$, is equal to $(X-1)W/X$, where W is the maximum length on the second principal axis direction of the area of spread of the total cell mixture. To get an approximation of the value of the area of spread of the labelled clone with X labelled cells, S_X , we assumed that the clone maximum lengths, L_X and W_X , are statistically independent of each other, and estimated the area of spread of a clone as the area of an ellipsoid, S_X , with expected value:

$$E(S_X) \sim \left(\frac{X-1}{X} \right)^2 S \quad (S4)$$

where S is the area of spread of the total mixture of interacting labelled and non-labelled cells. Supplementary Figure S5B shows that the clonal spread simulated by the agent-based model agrees with the theoretical spread of clone cells homogenously mixed with unlabelled cells given by Equation (S4), which proves that the computational model is correctly coded.

We next used Equation (S4) as an analytical term to capture the effect of spatial cell interactions at short range and of the proliferation potential of the founder cell on the spread of the labelled clone. According to Equation S4, the theoretical area of a labelled clone can be

estimated by $\left(\frac{X_i-1}{X_i} \right)^2 S$, where $X_i = 2^i$ is the number of labelled cells of a clone that

undertook i generations and S is the area of spread of the homogenous mixture of interacting labelled and non-labelled cells. We estimated S as the product of the cell area, σ , and the number of cells, both labelled and non-labelled, proliferating and interacting at short range, $S = \sigma (X_i)^\varepsilon$. Then, it follows that $(X_i)^\varepsilon = 2^{i\varepsilon}$ cells; in other words a clone with 2^i cells is in a homogenously mixed population of $2^{i\varepsilon}$ cells. The parameter ε quantifies a logarithmic ratio between the number of labelled and non-labelled cells interacting at short range. This parameter, therefore, captures the proliferation potential of the clone founder cell with respect to that of the neighbouring cell population spatially interacting at the short range. The cell proliferation potential can vary according to the duration of the division cycle, the number of undertaken generations or both growth parameters. The greater the value of ε , the smaller the proliferation potential of the clone founder labelled cell with respect to neighbouring cells.

An additional factor that can affect clone spread is organogenesis and assumed that the clone area increases isometrically as the intestine grows. We modelled the area of a cluster at the i th-generation, C_i , as the result of the area of the cluster at the immediately preceding birth time, C_{i-1} , multiplied by the factor by which the area of the intestine increases in that interval of time, which is the ratio I_i / I_{i-1} , and plus the increase in cluster area due to

the number of newly generated cells, which is equal to $\sigma X_i^\varepsilon \left(\frac{X_i-1}{X_i} \right)^2 - \sigma X_{i-1}^\varepsilon \left(\frac{X_{i-1}-1}{X_{i-1}} \right)^2$.

As shown in the Equation Summary box, these hypotheses lead to the following expression for the area of the cluster at the n -th average generation birth time, $C(X_n)$:

$$C(X_n) = \frac{I_n}{I_1} 2^\varepsilon \sigma \left(\frac{2-1}{2} \right)^2 + I_n \sigma \sum_{i=2}^n \frac{1}{I_i} \left(2^{i\varepsilon} \left(\frac{2^i-1}{2^i} \right)^2 - 2^{(i-1)\varepsilon} \left(\frac{2^{i-1}-1}{2^{i-1}} \right)^2 \right) \quad (S5)$$

Where $X_n = 2^n$, is the number of cells in the cluster at the n -th generation; I_i is the area of the small intestine at the i -th generation time, $1 \leq i \leq n$. Cell proliferation may eventually cease after n generations when the area of the intestine is equal to I_n ; once cell proliferation ceases, the growth of the intestine can continue. If during this non-proliferative period the area of the cluster increases isometrically with the area of the intestine, i.e. the area of the cluster is multiplied by the ratio I_n / I_{adult} , then:

$$C(X_{adult}) = \frac{I_{adult}}{I_1} 2^\varepsilon \sigma \left(\frac{2-1}{2} \right)^2 + I_{adult} \sigma \sum_{i=2}^n \frac{1}{I_i} \left(2^{i\varepsilon} \left(\frac{2^i-1}{2^i} \right)^2 - 2^{(i-1)\varepsilon} \left(\frac{2^{i-1}-1}{2^{i-1}} \right)^2 \right) \quad (S6)$$

Where $X_{adult} = X_n$ and I_{adult} , and C_{adult} , are the area of the intestine and cluster, respectively, in adulthood. It is straightforward to prove that if the intestine does not grow and cluster cells undertake n generations, the model in Equation (S6) predicts that the cluster area is equal to $\sigma 2^{n\varepsilon} \left(\frac{2^n-1}{2^n} \right)^2$. A simplification of the model in Equation (S6) is possible by assuming, in

agreement with the results presented here, that cell proliferation takes place at the time of labelling and that cell cycle duration is relatively short compared to the period of growth of the intestine so that the increase in the area of the intestine during the cell proliferation period can be disregarded. Thus, $I_i = I_l$ for each $2 \leq i \leq n$ and Equation (S6) reduces to:

$$C_{adult}(X_{adult}) = \frac{I_{adult}}{I_1} \sigma 2^{n\varepsilon} \left(\frac{2^n-1}{2^n} \right)^2 = \frac{I_{adult}}{I_1} \sigma X_n^\varepsilon \left(\frac{X_n-1}{X_n} \right)^2 \quad (S7)$$

Likewise, the length of a cluster, with X_i labelled cells, in either the longitudinal or circumferential axis direction can be modelled applying the same reasoning with a slight modification in the term accounting for the effect of the proliferation-driven interaction

between labelled and non-labelled cells on the cluster area from $\sigma X_i^\varepsilon \left(\frac{X_i-1}{X_i} \right)^2$ to

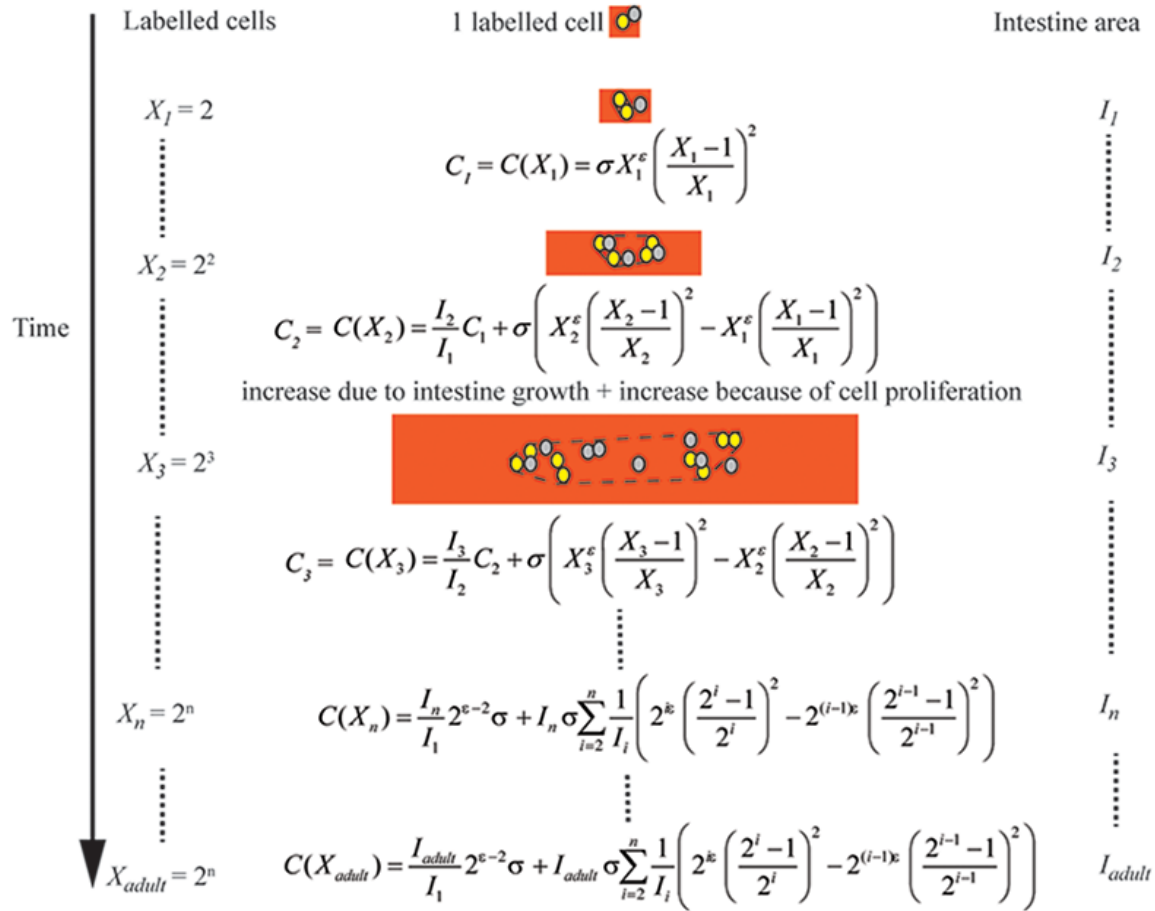
$\sqrt{\sigma X_i^\varepsilon} \left(\frac{X_i-1}{X_i} \right)$ in order to reflect the effect on its length.

Estimation of parameters of model in Equation (S7)

To parameterize Equation (S7) we have used experimental measurements of the area of the intestine at time E13.5, $I_l = 0.0866 \text{ cm}^2$, and in adult stage, $I_{adult} = 42.5 \text{ cm}^2$. We also

measured that the area of a cell was equal to $\sigma = 20 \mu\text{m}^2$, approximately, and assumed that this value was the same for all cell types.

The value of ε , which expresses that a population with X^ε cells contains X labelled cells of a given cell type, was estimated as $\varepsilon = \log(T)/\log(X)$ where, X , is the number of labelled cells and T is the total number of cells interacting. The estimation of T and X was based on the total counts of labelled cells observed in the adult intestine for cell types N, G and NG. These counts were equal to 78, 2140 and 2180 cells, respectively. If we assume that labelling is not biased for a determined cell type and considering that we have counted all labelled cells of each type in the adult intestine, those numbers should reflect the proportions of N, G and NG cells in the intestine. Hence, the value of ε for each clone type was estimated as $\varepsilon = \log(78+2140+2180)/\log(X)$ where X is the count of N, G or NG labelled cells in the adult intestine. This resulted in values of $\varepsilon = 1.92$ for the N-clone type and $\varepsilon = 1.09$ for both G- and NG- clone-types.



Equation Summary Box. Mathematical model of the area of spread of clones as a function of ENS cell progenitors proliferation and intestine growth during development. The model hypothesizes that the spread of a labelled clone depends on the growth of the intestine during development, on the proliferation potential of the founder cell and on cell proliferation-driven interactions between labelled (yellow) clone cells and non-labelled (grey) cells. The production of n consecutive generations of cells from an initial single labelled cell located on an intestine under continuous expansion is represented. $X_i = 2^i$, I_i and C_i represent the number of labelled cells, the area of the small intestine and of the spread of clone, respectively, at the birth time of the i -th generation of labelled cells; X_{adult} , I_{adult} and C_{adult} describe the same quantities in adulthood; σ denotes cell area; ϵ quantifies a logarithmic ratio between the number of labelled and non-labelled cells interacting at short range.

References and Notes

1. Y. Tanabe, T. M. Jessell, Diversity and pattern in the developing spinal cord. *Science* **274**, 1115–1123 (1996). [doi:10.1126/science.274.5290.1115](https://doi.org/10.1126/science.274.5290.1115) [Medline](#)
2. J. Furness, *The Enteric Nervous System* (Blackwell, 2006).
3. M. Avetisyan, E. M. Schill, R. O. Heuckeroth, Building a second brain in the bowel. *J. Clin. Invest.* **125**, 899–907 (2015). [doi:10.1172/JCI76307](https://doi.org/10.1172/JCI76307) [Medline](#)
4. C. Laranjeira, K. Sandgren, N. Kessaris, W. Richardson, A. Potocnik, P. Vanden Berghe, V. Pachnis, Glial cells in the mouse enteric nervous system can undergo neurogenesis in response to injury. *J. Clin. Invest.* **121**, 3412–3424 (2011). [doi:10.1172/JCI58200](https://doi.org/10.1172/JCI58200) [Medline](#)
5. S. Srinivas, T. Watanabe, C.-S. Lin, C. M. William, Y. Tanabe, T. M. Jessell, F. Costantini, Cre reporter strains produced by targeted insertion of EYFP and ECFP into the ROSA26 locus. *BMC Dev. Biol.* **1**, 4 (2001). [doi:10.1186/1471-213X-1-4](https://doi.org/10.1186/1471-213X-1-4) [Medline](#)
6. H. J. Snippert, L. G. van der Flier, T. Sato, J. H. van Es, M. van den Born, C. Kroon-Veenboer, N. Barker, A. M. Klein, J. van Rheenen, B. D. Simons, H. Clevers, Intestinal crypt homeostasis results from neutral competition between symmetrically dividing Lgr5 stem cells. *Cell* **143**, 134–144 (2010). [doi:10.1016/j.cell.2010.09.016](https://doi.org/10.1016/j.cell.2010.09.016) [Medline](#)
7. L. Madisen, T. A. Zwingman, S. M. Sunken, S. W. Oh, H. A. Zariwala, H. Gu, L. L. Ng, R. D. Palmiter, M. J. Hawrylycz, A. R. Jones, E. S. Lein, H. Zeng, A robust and high-throughput Cre reporting and characterization system for the whole mouse brain. *Nat. Neurosci.* **13**, 133–140 (2010). [doi:10.1038/nn.2467](https://doi.org/10.1038/nn.2467) [Medline](#)
8. A. Baggioini, S. Varum, J. M. Mateos, D. Bettosini, N. John, M. Bonalli, U. Ziegler, L. Dimou, H. Clevers, R. Furrer, L. Sommer, Premigratory and migratory neural crest cells are multipotent in vivo. *Cell Stem Cell* **16**, 314–322 (2015). [doi:10.1016/j.stem.2015.02.017](https://doi.org/10.1016/j.stem.2015.02.017) [Medline](#)
9. G. M. Kruger, J. T. Mosher, S. Bixby, N. Joseph, T. Iwashita, S. J. Morrison, Neural crest stem cells persist in the adult gut but undergo changes in self-renewal, neuronal subtype potential, and factor responsiveness. *Neuron* **35**, 657–669 (2002). [doi:10.1016/S0896-6273\(02\)00827-9](https://doi.org/10.1016/S0896-6273(02)00827-9) [Medline](#)
10. J. T. Mosher, K. J. Yeager, G. M. Kruger, N. M. Joseph, M. E. Hutchin, A. A. Dlugosz, S. J. Morrison, Intrinsic differences among spatially distinct neural crest stem cells in terms of migratory properties, fate determination, and ability to colonize the enteric nervous system. *Dev. Biol.* **303**, 1–15 (2007). [doi:10.1016/j.ydbio.2006.10.026](https://doi.org/10.1016/j.ydbio.2006.10.026) [Medline](#)
11. A. J. Bergner, L. A. Stamp, D. G. Gonsalvez, M. B. Allison, D. P. Olson, M. G. Myers Jr., C. R. Anderson, H. M. Young, Birthdating of myenteric neuron subtypes in the small intestine of the mouse. *J. Comp. Neurol.* **522**, 514–527 (2014). [doi:10.1002/cne.23423](https://doi.org/10.1002/cne.23423) [Medline](#)
12. W. Boesmans, R. Lasrado, P. Vanden Berghe, V. Pachnis, Heterogeneity and phenotypic plasticity of glial cells in the mammalian enteric nervous system. *Glia* **63**, 229–241 (2015). [doi:10.1002/glia.22746](https://doi.org/10.1002/glia.22746) [Medline](#)

13. H. M. Young, A. J. Bergner, T. Müller, Acquisition of neuronal and glial markers by neural crest-derived cells in the mouse intestine. *J. Comp. Neurol.* **456**, 1–11 (2003). [doi:10.1002/cne.10448](https://doi.org/10.1002/cne.10448) [Medline](#)
14. A. Chalazonitis, F. D'Autréaux, T. D. Pham, J. A. Kessler, M. D. Gershon, Bone morphogenetic proteins regulate enteric gliogenesis by modulating ErbB3 signaling. *Dev. Biol.* **350**, 64–79 (2011). [doi:10.1016/j.ydbio.2010.11.017](https://doi.org/10.1016/j.ydbio.2010.11.017) [Medline](#)
15. M. Rao, B. D. Nelms, L. Dong, V. Salinas-Rios, M. Rutlin, M. D. Gershon, G. Corfas, Enteric glia express proteolipid protein 1 and are a transcriptionally unique population of glia in the mammalian nervous system. *Glia* **63**, 2040–2057 (2015). [doi:10.1002/glia.22876](https://doi.org/10.1002/glia.22876) [Medline](#)
16. H. M. Young, C. J. Hearn, D. Ciampoli, B. R. Southwell, J.-F. Brunet, D. F. Newgreen, A single rostrocaudal colonization of the rodent intestine by enteric neuron precursors is revealed by the expression of Phox2b, Ret, and p75 and by explants grown under the kidney capsule or in organ culture. *Dev. Biol.* **202**, 67–84 (1998). [doi:10.1006/dbio.1998.8987](https://doi.org/10.1006/dbio.1998.8987) [Medline](#)
17. V. Sasselli, V. Pachnis, A. J. Burns, The enteric nervous system. *Dev. Biol.* **366**, 64–73 (2012). [doi:10.1016/j.ydbio.2012.01.012](https://doi.org/10.1016/j.ydbio.2012.01.012) [Medline](#)
18. T. A. Heanue, V. Pachnis, Expression profiling the developing mammalian enteric nervous system identifies marker and candidate Hirschsprung disease genes. *Proc. Natl. Acad. Sci. U.S.A.* **103**, 6919–6924 (2006). [doi:10.1073/pnas.0602152103](https://doi.org/10.1073/pnas.0602152103) [Medline](#)
19. D. Zhu, H. Xie, H. Li, P. Cai, H. Zhu, C. Xu, P. Chen, A. Sharan, Y. Xia, W. Tang, Nidogen-1 is a common target of microRNAs MiR-192/215 in the pathogenesis of Hirschsprung's disease. *J. Neurochem.* **134**, 39–46 (2015). [doi:10.1111/jnc.13118](https://doi.org/10.1111/jnc.13118) [Medline](#)
20. A. Jalali, A. G. Bassuk, L. Kan, N. Israsena, A. Mukhopadhyay, T. McGuire, J. A. Kessler, HeyL promotes neuronal differentiation of neural progenitor cells. *J. Neurosci. Res.* **89**, 299–309 (2011). [doi:10.1002/jnr.22562](https://doi.org/10.1002/jnr.22562) [Medline](#)
21. M. Caiazzo, S. Giannelli, P. Valente, G. Lignani, A. Carissimo, A. Sessa, G. Colasante, R. Bartolomeo, L. Massimino, S. Ferroni, C. Settembre, F. Benfenati, V. Broccoli, Direct conversion of fibroblasts into functional astrocytes by defined transcription factors. *Stem Cell Rep.* **4**, 25–36 (2015). [doi:10.1016/j.stemcr.2014.12.002](https://doi.org/10.1016/j.stemcr.2014.12.002) [Medline](#)
22. H. Zong, J. S. Espinosa, H. H. Su, M. D. Muzumdar, L. Luo, Mosaic analysis with double markers in mice. *Cell* **121**, 479–492 (2005). [doi:10.1016/j.cell.2005.02.012](https://doi.org/10.1016/j.cell.2005.02.012) [Medline](#)
23. T. Matsuoka, P. E. Ahlberg, N. Kessar, P. Iannarelli, U. Dennehy, W. D. Richardson, A. P. McMahon, G. Koentges, Neural crest origins of the neck and shoulder. *Nature* **436**, 347–355 (2005). [doi:10.1038/nature03837](https://doi.org/10.1038/nature03837) [Medline](#)
24. H. Enomoto, Death comes early: Apoptosis observed in ENS precursors. *Neurogastroenterol. Motil.* **21**, 684–687 (2009). [doi:10.1111/j.1365-2982.2009.01325.x](https://doi.org/10.1111/j.1365-2982.2009.01325.x) [Medline](#)
25. A. Schuchardt, V. D'Agati, L. Larsson-Blomberg, F. Costantini, V. Pachnis, Defects in the kidney and enteric nervous system of mice lacking the tyrosine kinase receptor Ret. *Nature* **367**, 380–383 (1994). [doi:10.1038/367380a0](https://doi.org/10.1038/367380a0) [Medline](#)

26. R. O. Heuckeroth, P. A. Lampe, E. M. Johnson Jr., J. Milbrandt, Neurturin and GDNF promote proliferation and survival of enteric neuron and glial progenitors in vitro. *Dev. Biol.* **200**, 116–129 (1998). [doi:10.1006/dbio.1998.8955](https://doi.org/10.1006/dbio.1998.8955) [Medline](#)
27. B. L. Cheeseman, D. Zhang, B. J. Binder, D. F. Newgreen, K. A. Landman, Cell lineage tracing in the developing enteric nervous system: Superstars revealed by experiment and simulation. *J. R. Soc. Interface* **11**, 20130815 (2014). [doi:10.1098/rsif.2013.0815](https://doi.org/10.1098/rsif.2013.0815) [Medline](#)
28. A. J. Burns, N. M. Le Douarin, Enteric nervous system development: Analysis of the selective developmental potentialities of vagal and sacral neural crest cells using quail-chick chimeras. *Anat. Rec.* **262**, 16–28 (2001). [doi:10.1002/1097-0185\(20010101\)262:1<16:AID-AR1007>3.0.CO;2-O](https://doi.org/10.1002/1097-0185(20010101)262:1<16:AID-AR1007>3.0.CO;2-O) [Medline](#)
29. D. Kim, G. Pertea, C. Trapnell, H. Pimentel, R. Kelley, S. L. Salzberg, TopHat2: Accurate alignment of transcriptomes in the presence of insertions, deletions and gene fusions. *Genome Biol.* **14**, R36 (2013). [doi:10.1186/gb-2013-14-4-r36](https://doi.org/10.1186/gb-2013-14-4-r36) [Medline](#)
30. Y. Liao, G. K. Smyth, W. Shi, featureCounts: An efficient general purpose program for assigning sequence reads to genomic features. *Bioinformatics* **30**, 923–930 (2014). [doi:10.1093/bioinformatics/btt656](https://doi.org/10.1093/bioinformatics/btt656) [Medline](#)
31. R Core Team, R: A language and environment for statistical computing (R Foundation for Statistical Computing, 2016); www.R-project.org/.
32. F. Buettner, K. N. Natarajan, F. P. Casale, V. Proserpio, A. Scialdone, F. J. Theis, S. A. Teichmann, J. C. Marioni, O. Stegle, Computational analysis of cell-to-cell heterogeneity in single-cell RNA-sequencing data reveals hidden subpopulations of cells. *Nat. Biotechnol.* **33**, 155–160 (2015). [doi:10.1038/nbt.3102](https://doi.org/10.1038/nbt.3102) [Medline](#)
33. W. Boesmans, M. A. Martens, N. Weltens, M. M. Hao, J. Tack, C. Cirillo, P. Vanden Berghe, Imaging neuron-glia interactions in the enteric nervous system. *Front. Cell. Neurosci.* **7**, 183 (2013). [doi:10.3389/fncel.2013.00183](https://doi.org/10.3389/fncel.2013.00183) [Medline](#)
34. D. G. Gonsalvez, M. Li-Yuen-Fong, K. N. Cane, L. A. Stamp, H. M. Young, C. R. Anderson, Different neural crest populations exhibit diverse proliferative behaviors. *Dev. Neurobiol.* **75**, 287–301 (2015). [doi:10.1002/dneu.22229](https://doi.org/10.1002/dneu.22229) [Medline](#)